ASAIO Journal Publish Ahead of Print

DOI: 10.1097/MAT.0000000000000559

The Effect Of Inlet Cannula Length On The Intraventricular Flow Field *An In Vitro* Flow Visualization Study Using The Evaheart LVAD

Karen May-Newman, Ph.D.[1], Juyeun Moon[1], Varsha Ramesh, M.S. [1], Ricardo Montes[1], Josue Campos[1], Brian Herold[1], Paul Isingoma[1], Tadashi Motomura, M.D. [2] and Robert Benkowski [3]

[1] Bioengineering Program, San Diego State University, San Diego, CA 92182-1323

[2] Evaheart, Inc., Houston, TX 77030

[3] B-Squared Medical Device Solutions, Fort Worth TX 76109

Corresponding Author:

Karen May-Newman, Ph.D.

Professor of Mechanical Engineering

San Diego State University

5500 Campanile Dr.

San Diego, CA 92182-1323

Conflicts of Interest and Source of Funding: K. May-Newman is a consultant for B-Squared Medical Device Solutions. Funding for this project was received from Evaheart, Incc.

Acknowledgements

The authors appreciate the suggestions of Dr. Steve Reichenbach, as well as the assistance of Claudine Reider, M.S. Funding for this study was obtained from Evaheart, Inc.

Abstract

LVAD inflow cannula malposition is a significant risk for pump thrombosis. Thrombus development is influenced by altered flow dynamics, such as stasis or high shear that promote coagulation. The goal of this study was to measure the intraventricular flow field surrounding the apical inflow cannula of the Evaheart centrifugal LVAD, and assess flow stasis, vortex structures and pulsatility for a range of cannula insertion depths and support conditions. Experimental studies were performed using a mock loop with a customized silicone left ventricle (LV) and the Evaheart LVAD. A transparent inflow cannula was positioned at 1cm, 2cm, or 3cm insertion depth into the LV and the velocity field in the LV midplane was measured for two levels of LVAD support: 1800rpm and 2300rpm. The LV velocity field exhibits a diastolic vortex ring whose size, path and strength are affected by the flow conditions and cannula position. During diastole, the large clockwise midplane vortex grows, but its circulation and kinetic energy are reduced with cannula insertion depth. The counter-clockwise vortex is smaller and exhibits more complex behavior, reflecting a flow split at 3cm. Overall, the 1cm cannula insertion depth produces the flow pattern that exhibits the least apical flow stasis and greatest pulsatility and should correlate to a lower risk of thrombus formation.

Introduction

Abnormal blood flow patterns including both stagnation and turbulence are linked with thromboembolic events, especially in the presence of medical devices [1,2]. In particular, left ventricular assist devices (LVADs) provide tremendous benefits for patients by reducing the symptoms of heart failure (HF), however, 17-20% of LVAD patients have a stroke within the first year of implantation[3], and 25% have a major bleeding event requiring hospitalization[4–6]. Thus, LVAD recipients present unique challenges in thromboembolic (TE) management. A balance must be achieved among the mechanical settings of the LVAD, the anticoagulation strategy, and the responsiveness of the patients myocardium to pharmacologic therapy [7].

Previous studies have demonstrated that blood flow in the normal healthy left ventricle (LV) is unsteady, 3-D and exhibits a range of different length scales [8–10]. Most have found a common flow pattern consisting of a large diastolic vortex that channels the transit of blood towards the aortic valve [11–14]. This vortex has been shown to contribute to diastolic suction [15], and to minimize kinetic energy losses and cardiac work [16]. The LV vortex has also been shown to facilitate the blood mass coming into the LV during one beat washing out completely after a few beats [17], which prevents intraventricular blood stagnation [13]. During the development of HF, the heart progressively dilates as part of hemodynamic compensation to provide sufficient blood flow to the end-organs. In patients with cardiac dysfunction, changes in both geometry and function create shorter, rounder vortex structures that have lower strength and persistence [15,18,19]. These patterns have been associated with greater energy dissipation and reduced blood transport than in the normal heart, further decreasing efficiency in the compromised patient [20].

The current generation of continuous flow LVADs changes the blood flow path through the heart, introducing alterations in the natural flow pattern that are associated with TE [21–23] complications. The LVAD inflow cannula is typically located at the LV apex, and the outlet conduit anastomoses to the ascending aorta, bypassing the aortic valve. Implantation of the LVAD provides an immediate increase in systemic blood flow and end-organ perfusion, providing an alternate pathway for blood to flow from

the heart to the arterial system. LVAD support unloads the heart, decreasing the magnitude and pulsatility of LV pressure, which can fall below the level needed to fully open the aortic valve during myocardial contraction. In many LVAD patients, blood flow occurs entirely through the LVAD, the aortic valve is continuously closed and the heart operates *in series* with the pump. Decreased pulsatility accompanies continuous flow LVAD support, which exacerbates the mixing of blood, decreasing the washout of the LV outflow tract and the aortic root. Our previous studies have measured the flow field in a model of the LVAD-assisted heart and found that LVAD support does not disrupt the formation of the intraventricular vortex, but the vortex dissipates more quickly with increased LVAD speed [23]. LVAD support decreases or eliminates aortic valve opening, altering the path of blood through the heart which creates areas of stasis that are at risk for thrombus formation.

One region prone to TE complications identified in previous studies is the ventricular apex, near the LVAD inflow cannula[24,25]. The positioning of the inflow cannula has been shown to be important for proper LV flow. Previous studies have identified cannula malposition as a significant risk for pump thrombosis [26,27]. During the placement of the LVAD, it is important to angulate the inflow cannula to avoid obstruction, which can occur if the cannula is angled rather than parallel to the intraventricular septum. Taghavi et al demonstrated that patients with thrombus had more angulated inflow cannula from a horizontal line (48 vs. 65) and a shallower pump pocket than those without thrombus [27]. Adamson and colleagues identified best practices associated with low thrombus incidence, which includes inflow cannula positioning consistent with the non-thrombus cohort of the Taghavi study [26,28,29]. Thrombus due to the healing of the apical core ("wedge thrombus") occurs during the early post-operative period, usually within 3 months. If the inflow cannula touches the LV septum or free wall, then the resulting pannus formation and/or inflow occlusion could occur throughout the duration of support. Thrombus development is exacerbated by altered flow dynamics, which can produce areas of flow stasis or high shear that promote coagulation. Thus, inflow cannula positions that produce more stasis or velocity gradients, especially adjacent to the cannula, are likely to exhibit greater thrombogenicity.

A change in cannula design or position should thus assess alterations introduced into the intraventricular flow field that may exacerbate the risk of thrombus formation and growth. The goal of this study was to visualize the intraventricular flow field surrounding the apical inflow cannula of the Evaheart centrifugal LVAD, and assess flow stasis and mixing for a range of cannula lengths and support conditions. The resulting data will apply to better understanding the dynamics and interaction of the inflow cannula not only with the healing myocardium (acute period, full support) but also during chronic (partial) support, and how these could inform on TE complications including stroke and pump thrombosis.

Methods

Experimental studies were performed with the SDSU cardiac simulator (CS), a mock loop designed to reproduce the flow conditions of the LVAD-assisted heart [23,30]. Customized transparent models of a dilated LV were fabricated from platinum-cured silicone rubber based on the idealized geometry of a heart failure patient LV. The LV model has an idealized geometry, as shown in Figure 1, which is designed to remain inflated, without wrinkles or creases, during the study. Medtronic 305 Cinch bio-prosthetic porcine aortic valves were used in both aortic and mitral valve positions. A clear polished polycarbonate version of the LVAD inflow cannula (16 mm ID, 20 mm OD) was fabricated for flow visualization, and was longer than the normal cannula in order to allow for insertion into the LV as part of the study. A Evaheart LVAD (Evaheart, Inc.; Houston TX) was attached to the inflow cannula, and the outflow graft replaced with Tygon tubing with the same inner diameter, which was connected to the ascending aorta (Figure 1).

The assembly is immersed in a water-filled tank and connected to a Windkessel model of the circulation [23]. The fluid surrounding the LV model is pressurized in a cyclic manner, causing the LV to "beat" at 70 bpm. The circulating fluid is a viscosity-matched blood analog consisting of 40% glycerol and saline. Pressure and flow transducers are used to record the following hemodynamic variables at 200 Hz using a data acquisition system (LabChart, AD Instruments): LV pressure (LVP), aortic root pressure

(AoP), LVAD flow rate (Q-LVAD), and distal aortic flow rate (Q-Total). Ten cycles, recorded during imaging, were averaged for each flow condition.

The velocity field in the LV midplane, *v(x,y)*, was measured with Digital Particle Image Velocimetry (DPIV), an engineering method that uses a thin (1-2mm) laser light sheet to illuminate small (20 μm) fluorescent particles (PMMA-RhB) which are imaged and analyzed for motion using a LaVision DPIV system (LaVision, Inc) [31]. The camera (LaVision Imager Intense) recorded 12-bit digital images with a time interval of 700-1200μs based on the average velocity of the flow field. A sequential acquisition technique that phase-locked specific phases of the cardiac cycle based on predefined LVP profiles was used to match time points during the cardiac cycle [23]. Triggered image pairs were acquired at 40 Hz for each condition and ten image sets collected for each time point and phase averaged. The image field was calibrated using a grid with 2-mm spacing covering the field of view. A mask corresponding to the LV boundary was generated at each time frame and applied to remove the image background. Interrogation windows of 32x32 were applied to a field of 1376x1040 pixels to obtain sufficient spatial resolution (14 pixels/mm) in the calculation of the 2-D velocity field in the LV midplane, *v(x,y)*.

A baseline condition was established to simulate a pre-LVAD patient, with the LVAD off and the LVAD conduit clamped. The baseline hemodynamics target an AoP of 60 ± 4 mmHg and a Q-total of 3.5 ± . 3 L/min, representative of HF patients with a severity level of NYHA IV [32,33]. The baseline is established by adjusting the resistance and compliance of the cardiac simulator and then maintained constant for the duration of the study.

The velocity field was evaluated for a range of clinical conditions represented by parallel flow, during which a significant portion of the LV flow is ejected through the native aortic valve, and series flow, during which the aortic valve is continuously closed and all blood exits through the LVAD. These conditions were represented by LVAD speeds of 1800 and 2300 rpm, respectively. Three different cannula positions were examined, corresponding to insertion depths of 1, 2 and 3 cm into the LV through the apex, and designated C_1, C_2, and C_3, respectively. For each cannula position, the study

was repeated twice – once with the camera positioned to view the full LV model, and another with the camera positioned closer to the model for a higher resolution image of the flow field at the LV apex. Each time the camera or the LV model was repositioned, the system was recalibrated to ensure an accurate reconstruction from the images. The PIV measurements yielded a average cardiac cycle consisting of 36 images for each of the six test flow conditions.

Data Analysis. Velocity field data, *v(x,y)*, were further analyzed to calculate indices of fluid stasis and vortex structures. Small user-defined regions of interest are evaluated for mean velocity during the cardiac cycle as a way of assessing differences across the various flow conditions. A rectangular region of at least 50 pixels is selected on the image and the average velocity calculated for each frame during the cardiac cycle. A map of localized pulsatility index was developed by evaluating the maximum and minimum velocity values for each point in the PIV data grid, then dividing that local value by the mean for the entire velocity over the full cardiac cycle:

$$PI = \frac{(v_{max} - v_{min})}{v_{ave}}$$

Vortex identification enables visualization and quantification of swirling coherent structures. In 2-D, the three-dimensional (3-D) LV vortex ring is visualized as two cores corresponding to the intersections between the diastolic vortex ring and the imaging plane, with the clockwise rotating vortex (main) directed toward the anteroseptal wall and the counterclockwise (secondary) vortex close to the inferolateral LV wall. In-plane properties of the tracked vortex cores were determined from the velocity data obtained on the imaging plane using a MATLAB analysis. The details of this analysis are described in the Appendix.

Following previous studies [19], we defined an orthogonal anatomical reference system of the LV as the intersection of the long axis of the ventricle with the line that passes through the mitral annulus and the aortic tract. Vortex positions in this system were normalized by the long (range: 0 (mitral base) –1 (apex)) and short (range:-0.5 to 0.5) axes. The temporal waveforms for the radius, position, circulation,

and in-plane KE were obtained for the full cardiac cycle for both main and secondary vortices. The distance from the vortex center to the base of the aortic valve was calculated and divided by the long axis distance to compute a normalized apex-base distance (NBAD) which is a measure of relative vortex depth in the LV. Mean values for the cardiac cycle as well as instantaneous values at each cardiac event were measured from these waveforms.

Results:

The results of the average hemodynamics of the system are reported in Table 1, which shows that the baseline distal aortic flow rate of 3.5 L/min increases to 4.3 L/min at an LVAD speed of 1800 rpm, during which the LVAD provides approximately 75% of the flow. A further increase in LVAD speed to 2300 rpm brings the flow rate to 5.3 L/min, with all of the flow exiting the LV through the LVAD. The hemodynamics of the different flow conditions were fairly consistent across the three different cannula positions (C_1, C_2, and C_3) and 2 views (Large, Zoom – data not shown), although a slight but consistent increase in the fraction of flow through the LVAD was observed at 1800 rpm as the cannula length increased. The table of hemodynamics confirms that the flow conditions were closely matched for all cannula positions at the same LVAD speed setting. As LVAD speed increases, the pulsatility of both the aortic flow and LVAD flow are reduced. Aortic pulsatility index (PI) reduces primarily due to a decrease in the maximum aortic flow rate, and LVAD pulsatility index decreases by an increase in the minimum LVAD flow rate.

Figure 2 provides a sequence of velocity field images for each cannula position that are closely matched for four time points during the cardiac cycle. Figure 2A illustrates the nonphysiological baseline condition, in which the LVAD is off and the tubing is clamped. The second sequence (Figure 2B) shows the velocity field for the parallel flow conditions (LVAD speed of 1800rpm), and the third (Figure 2C) depicts the series condition (LVAD speed of 2300 rpm). The sequences begin with early diastole, showing the vortex ring at it enters the LV through the mitral valve. As diastole progresses, the growth of the anterior vortex is interrupted by the cannula in the C_2 and C_3 positions, although the

C_3 position produces a flow splitting that creates increased washing around the cannula and towards the apex. The cannula restricts the movement of the vortex within the ventricle, but the formation and persistence of the CW and CCW vortices resemble the normal heart. During systole, most of the circulating fluid is ejected through the LVAD conduit, which is reflected in the last panel.

The apical regions of stasis adjacent to the inflow cannula were further analyzed to compare the different cannula positions at both 1800 and 2300 rpm LVAD speeds. Figure 3 shows the position of the two regions of interest, ROI#1 (septal side of the cannula) and ROI#2 (free wall side) on the LV model and the time series of their average velocity in the plots below. The pattern in ROI#1 begins with small increase in velocity during systole, followed by a larger increase – at least for the C_1 position – during diastole. ROI#2 reflects less flow during systole, but attains higher values during diastole than ROI#1. The results for ROI#1 show little difference between C_ 2 and C_3, however ROI#2 reflects the flow field split for the C_3 position that reaches velocities similar to C_ 1. This flow split washes the apical region adjacent to the LV free wall, and appears not to be present at C_ 2. Thus, the results indicate that C_! and C_ 3 have the highest washing in these regions. These trends are also reflected in the velocity averaged over the cardiac cycle as shown. The washing of the inner surface of the LVAD cannula, and the LVAD in general, is illustrated in the PI color map of Figure 4. The PI maps highlight the areas of apical stasis affected by cannula position. All cannula positions show some level of diminished maximum velocity and pulsatility near the junction of the cannula and apex.

Figure 5 shows the circulation of the clockwise (CW) and counter-clockwise (CCW) vortex cores during the cardiac cycle. Both LVAD speeds show similar timing, and reflect some differences in vortex formation for the different cannula positions. The vortex forms and grows during diastole, generating a large rise in circulation following systole. Vortex circulation is positive for the CW vortex, and negative for the CCW vortex, with the CW vortex exhibiting the greatest circulation. A second bump in vortex circulation is observed towards the end of diastole, which corresponds to the A wave. Peak circulation is greatest for the C_1 position for both CW and CCW vortices, followed by C_2 and C_3 in order.

However, the average values shown in Table 2 do not reflect the large variations that occur during the cardiac cycle. Vortex kinetic energy is affected by both cannula position and LVAD speed. Increased LVAD speed produces a slight but consistent increase in CCW vortex KE, as well as a noticeable decrease in CW vortex KE at C_ 3. CW vortex KE for C_3 was substantially lower than the other two positions, and CCW KE was substantially higher for C_2 than for the other two positions. The CW vortex becomes more elliptical with cannula insertion, and the CCW becomes bigger.

Discussion

This study of the effect of inflow cannula position on intraventricular flow dynamics in the LVAD-assisted heart provides some quantitative measures that enable comparison of the potential risk of TE events. However, there are many assumptions inherent in the experimental setup, and the extension of fluid mechanics to coagulation is based on general principles such as Virchow's triad. Because Virchow's triad also includes factors such as the blood coagulation state and the exposure to artificial surfaces, which vary widely among patients, any trends indicated by experimental measurements must be validated with clinical data. In addition, the relationship of vortex formation and fluid velocity in the midplane of the LV does not capture the full 3-D nature of the flow field, or account for the residence time of particles as they pass through the LV. The cardiac simulator has other limitations as mentioned previously, but provides a reproducible testbed for exploring the interaction of the LVAD with the native circulation.

The results of the present study indicate that flow alterations arise as the inflow cannula is inserted further into the LV. Vortex formation is affected, with the CW vortex showing reduced circulation with cannula insertion and a flow split that occurs when the cannula is inserted the farthest that appears to improve CCW vortex transport and decrease stasis near the apex. A comparison of the vortex properties with published values for normal healthy controls and patients with dilated cardiomyopathy (Table 2) shows that the flow patterns in our model produce values closer to those of the DCM heart, reflecting the enlarged geometry of the silicone LV.

The results of this study can be applied to understanding the LV flow dynamics during LVAD support with other pump designs, such as the HeartMate II, HeartWare HVAD, and MVAD, taking into account variations in cannula diameter and differences in pump design that affect the H-Q curve. For some cannula designs, however, the shape of the cannula tip and the presence of texturing on the titanium surface may preclude simple changes in the intended cannula depth and limit the direct relevance of our findings.

The authors speculate that both hypo and hyper volemic states would alter both the volume and the flow patterns within the LV. With hypovolemia, we speculate adecreased end diastolic volume (given the same pump speed) and reduced diastolic vortices in the LV. In this case, with reduced washout of the inflow cannula root, a shorter insertion length would be less susceptible to forming a wedge thrombus. With hypervolemia, there is an increased risk of LVAD suction and again, a shorter inflow length is expected to be less susceptible to occlusion with the LV than a longer insertion length. With brady-tachy cardia, and hypo-hyper tension, it is expected the flow patterns would be similar to what has been demonstrated except with varying degrees of magnitude. These areas of investigation are planned for future studies.

The study has some limitations, due to the inability of the *in vitro* cardiac simulator to include some aspects of physiological control, including autoregulation and the Frank-Starling response. In addition, the flow in the heart is three-dimensional, featuring a vortex ring of which only a two-dimensional slice is measured in our studies. However, the vortex, flow and stasis indices correlate well with patient studies under matched geometry and flow conditions[19,34], thus providing a platform for reliable measurements of how the fluid mechanics are likely to change with LVAD inflow cannula position in patients under matched flow conditions. The design of the system is based on simulating a heart failure model, using a dilated LV model and a low ejection fraction. The simulator does not apply twist to the LV, an important feature of normal biomechanics but one which is greatly diminished in patients with dilated cardiomyopathy[35,36]. It has been recently been suggested that reduction of twist is one of the

pathological mechanisms that progresses heart failure. Reduced rotation at both base and apex, exacerbated by myocardial fibrosis, produces a decrease in LV twist[36]. Twist is further decreased by the surgical attachment to the LVAD inflow cannula, which constrains rotational motion.

The study is focused on assessing the effect of cannula insertion depth on the LV flow field, without any other geometrical changes, either in the heart or the LVAD cannula positioning such as angulation. The impact of cannula angle on the flow field will be assessed in a subsequent study, with an added focus of suction and LV remodeling, which adds clinical relevance beyond the experimental design of the present study. In the native heart, reverse remodeling of the LV occurs in many LVAD patients, over weeks or months following the implant surgery. This remodeling generally results in decreased LV volume and increased ejection fraction[7], both which improve blood transport beyond the effect of the LVAD. Studies designed to investigate reverse remodeling using the simulator are currently underway.

Conclusion

This study provides mechanistic insight into the high incidence of thrombus formation observed with LVAD support that manifests as serious clinical events such as stroke and pump malfunction. The position of the LVAD inflow cannula has long been recognized as a critical influence on thrombus formation via the introduction of flow abnormalities that activate blood components, but a lack of quantitative studies have delayed the evidence-based strategies to overcome these obstacles. By simulating the cardiovascular system *in vitro,* we can isolate and control each variable affecting LV flow and tease out the targets for improvement through a systematic engineering-based approach. Quantification of local velocity, pulsatility, and vortex dynamics has never been applied to the optimization of cannula placement and this study serves as a foundation for future comparisons of cannula orientation and size, LVAD design, and pulsatility algorithms.

The findings illustrate the LV flow fields during LVAD support for three cannula insertion depths, and evaluate the effect on local and global washing of the LV cavity. All cannula positions demonstrate diminished washing near to the cannula insertion site at the apex, a site at which thrombus formation has

been found in clinical studies[24]. Overall, the C_1 cannula position produces the flow pattern that exhibits the least apical flow stasis and greatest pulsatility and should correlate to a lower risk of TE complications. Although dependent on LVAD speed and particular location, the vortex properties indicate that C_1 produces the least alteration to the vortex pattern during LVAD support. The authors propose that the short insertion into the LV may actually be less susceptible for risk of misalignment. If the inflow cannula pivots at the sewing ring attachment to the epicardium and given the same angle of misalignment, with a shorter insertion, the absolute tip motion is less than if the insertion length is longer. The clinical significance of the differences observed in the flow field will be dependent on other factors such as the cannula material and surface characteristics, as well as the patient's coagulation status. Future studies are planned to evaluate cannula angulation with both axial and centrifugal LVADs to further assess differences in flow and transport.

References

1. Goswami KC, Yadav R BVK. Predictors of left atrial appendage clot: a transesophageal echocardiographic study of left atrial appendage function in patients with severe mitral stenosis. *Indian Hear J*. 2004;56((6)):628-635.
2. Bluestein D. Research approaches for studying flow-induced thromboembolic complications in blood recirculating devices. *Expert Rev Med Devices*. 2004;1(1):65-80. doi:10.1586/17434440.1.1.65.
3. Petrucci RJ, Rogers JG, Blue L, et al. Neurocognitive function in destination therapy patients receiving continuous-flow vs pulsatile-flow left ventricular assist device support. *J Hear Lung Transplant*. 2012;31(1):27-36. doi:10.1016/j.healun.2011.10.012.
4. Harvey L, Holley CT, John R. Gastrointestinal bleed after left ventricular assist device implantation: incidence, management, and prevention. *Ann Cardiothorac Surg*. 2014;3(5):475-479. doi:10.3978/j.issn.2225-319X.2014.08.19.
5. Lopilato AC, Doligalski CT, Caldeira C. Incidence and Risk Factor Analysis for Gastrointestinal Bleeding and Pump Thrombosis in Left Ventricular Assist Device Recipients. *Artif Organs*. 2015;39(11):939-944. doi:10.1111/aor.12471.
6. Whitson BA, Eckman P, Kamdar F, et al. Hemolysis, pump thrombus, and neurologic events in continuous-flow left ventricular assist device recipients. *Ann Thorac Surg*. 2014;97(6):2097-2103. doi:10.1016/j.athoracsur.2014.02.041.
7. Drakos SG, Wever-Pinzon O, Selzman CH, et al. Magnitude and Time Course of Changes Induced by Continuous-Flow Left Ventricular Assist Device Unloading in Chronic Heart Failure. *J Am Coll Cardiol*. 2013;61(19):1985-1994. doi:10.1016/j.jacc.2013.01.072.
8. Bolger AF, Heiberg E, Karlsson M, et al. Transit of blood flow through the human left ventricle mapped by cardiovascular magnetic resonance. *J Cardiovasc Magn Reson*. 2007;9(5):741-747. doi:10.1080/10976640701544530.

9. Eriksson J, Carlhäll CJ, Dyverfeldt P, Engvall J, Bolger AF, Ebbers T. Semi-automatic quantification of 4D left ventricular blood flow. *J Cardiovasc Magn Reson*. 2010;12:9. doi:10.1186/1532-429X-12-9.

10. Hendabadi S, Bermejo J, Benito Y, et al. Topology of blood transport in the human left ventricle by novel processing of Doppler echocardiography. *Ann Biomed Eng*. 2013;41(12):2603-2616. doi:10.1007/s10439-013-0853-z.

11. Kheradvar A, Houle H, Pedrizzetti G, et al. Echocardiographic particle image velocimetry: a novel technique for quantification of left ventricular blood vorticity pattern. *J Am Soc Echocardiogr*. 2010;23(1):86-94. doi:10.1016/j.echo.2009.09.007.

12. Kim WY, Walker PG, Pedersen EM, et al. Left ventricular blood flow patterns in normal subjects: a quantitative analysis by three-dimensional magnetic resonance velocity mapping. *J Am Coll Cardiol*. 1995;26(1):224-238. http://www.ncbi.nlm.nih.gov/pubmed/7797756.

13. Hong G-R, Pedrizzetti G, Tonti G, et al. Characterization and quantification of vortex flow in the human left ventricle by contrast echocardiography using vector particle image velocimetry. *JACC Cardiovasc Imaging*. 2008;1(6):705-717. doi:10.1016/j.jcmg.2008.06.008.

14. Martinez-Legazpi P, Bermejo J, Benito Y, et al. Contribution of the diastolic vortex ring to left ventricular filling. *J Am Coll Cardiol*. 2014;64(16):1711-1721. doi:10.1016/j.jacc.2014.06.1205.

15. Kheradvar A, Milano M, Gharib M. Correlation between vortex ring formation and mitral annulus dynamics during ventricular rapid filling. *ASAIO J*. 2007;53(1):8-16. doi:10.1097/01.mat.0000249870.44625.22.

16. Pedrizzetti G, Domenichini F. Nature Optimizes the Swirling Flow in the Human Left Ventricle. *Phys Rev Lett*. 2005;95(10):1-4. doi:10.1103/PhysRevLett.95.108101.

17. Watanabe H, Sugiura S, Hisada T. The looped heart does not save energy by maintaining the momentum of blood flowing in the ventricle. *Am J Physiol Heart Circ Physiol*. 2008;294(5):H2191--6. doi:10.1152/ajpheart.00041.2008.

18. Loerakker S, Cox LGE, van Heijst GJF, de Mol B a JM, van de Vosse FN. Influence of dilated cardiomyopathy and a left ventricular assist device on vortex dynamics in the left ventricle. *Comput Methods Biomech Biomed Engin*. 2008;11(6):649-660. doi:10.1080/10255840802469379.

19. Bermejo J, Benito Y, Alhama M, et al. Intraventricular vortex properties in nonischemic dilated cardiomyopathy. *Am J Physiol Heart Circ Physiol*. 2014;306(5):H718-29. doi:10.1152/ajpheart.00697.2013.

20. Faludi R, Szulik M, D'hooge J, et al. Left ventricular flow patterns in healthy subjects and patients with prosthetic mitral valves: an in vivo study using echocardiographic particle image velocimetry. *J Thorac Cardiovasc Surg*. 2010;139(6):1501-1510. doi:10.1016/j.jtcvs.2009.07.060.

21. Fyrenius A, Wigström L, Ebbers T, Karlsson M, Engvall J, Bolger AF. Three dimensional flow in the human left atrium. *Heart*. 2001;86(4):448-455. doi:10.1136/heart.86.4.448.

22. Girdhar G, Xenos M, Alemu Y, et al. Device thrombogenicity emulation: a novel method for optimizing mechanical circulatory support device thromboresistance. *PLoS One*. 2012;7(3):e32463. doi:10.1371/journal.pone.0032463.

23. Wong K, Samaroo G, Ling I, et al. Intraventricular flow patterns and stasis in the LVAD-assisted heart. *J Biomech*. 2014;47(6):1485-1494. doi:10.1016/j.jbiomech.2013.12.031.

24. Strickland KC, Watkins JC, Couper GS, Givertz MM, Padera RF. Thrombus around the redesigned HeartWare HVAD inflow cannula: a pathological case series. *J Hear Lung Transplant*. 2016;in press:1-4. doi:10.1016/j.healun.2016.01.1230.

25. Son J-W, Park W-J, Choi J-H, et al. Abnormal Left Ventricular Vortex Flow Patterns in Association With Left Ventricular Apical Thrombus Formation in Patients With Anterior Myocardial Infarction. *Circ J*. 2012;76(11):2640-2646. doi:10.1253/circj.CJ-12-0360.

26. Farrar DJ, Ph D, Dembitsky WP, et al. Principles of HeartMate II implantation to avoid pump

malposition and migration. *J Card Surg*. 2015;30(February):296-299. doi:10.1111/jocs.12478.

27. Taghavi S, Ward C, Jayarajan SN, et al. Surgical technique influences HeartMate II left ventricular assist device thrombosis. *Ann Thorac Surg*. 2013;96(4):1259-1265.

28. Klodell CT, Massey HT, Adamson RM, et al. Factors related to pump thrombosis with the Heartmate II left ventricular assist device. *J Card Surg*. 2015;30:775-780.

29. Adamson RM, Bower BL, Sundareswaran KS, Farrar DJ, Dembitsky WP. Radiologic assessment of HeartMate II position: Minimal pump migration after long-term support. *J Hear Lung Transplant*. 2015;34(12):1617-1623. doi:10.1016/j.healun.2015.07.006.

30. Zamarripa Garcia M a, Enriquez L a, Dembitsky W, May-Newman K. The effect of aortic valve incompetence on the hemodynamics of a continuous flow ventricular assist device in a mock circulation. *ASAIO J*. 2008;54(3):237-244. doi:10.1097/MAT.0b013e31816a309b.

31. Willert CE, Gharib M. Digital particle image velocimetry. *Exp Fluids*. 1991;193(4):181-193. doi:10.1007/BF00190388.

32. Maurer MM, Burkhoff D, Maybaum S, et al. A Multicenter Study of Noninvasive Cardiac Output by Bioreactance During Symptom-limited Exercise. *J Card Fail*. 2009;15(8):689-699. doi:10.1016/j.cardfail.2009.04.005.

33. Travis AR, Giridharan G a., Pantalos GM, et al. Vascular pulsatility in patients with a pulsatile- or continuous-flow ventricular assist device. *J Thorac Cardiovasc Surg*. 2007;133(2):517-524. doi:10.1016/j.jtcvs.2006.09.057.

34. Rossini L, Martinez-Legazpi P, Vu V, et al. A Clinical Method for Mapping and Quantifying Blood Stasis in the Left Ventricle. *J Biomech*. 2016;49(11):2152-2161. doi:http://dx.doi.org/10.1016/j.jbiomech.2015.11.049.

35. Dalen BM Van, Kauer F, Vletter WB, et al. Influence of cardiac shape on left ventricular twist. *J Appl Physiol*. 2010;108:146-151. doi:10.1152/japplphysiol.00419.2009.

36. Kauer F, Geleijnse ML, Dalen BM Van, Kauer F, Geleijnse ML, Martijn B. Role of left

ventricular twist mechanics in cardiomyopathies, dance of the helices. *World J Cardiol*. 2015;7(8):476-483. doi:10.4330/wjc.v7.i8.476.

37. Chakraborty P, Balchandar S, Adrian RJ, Balachandar S, Adrian RJ. On the relationships between local vortex identification schemes. *J Fluid Mech*. 2005;535:189-214. doi:10.1017/S0022112005004726.

38. Garcia D, Juan JC, Tanné. D, et al. Two-dimensional intraventricular flow mapping by digital processing conventional color-doppler echocardiography images. *IEEE Trans Med Imaging*. 2010;29(10):1701-1713. doi:10.1109/TMI.2010.2049656.

Figure Legends

Figure 1. The SDSU cardiac simulator is a mock circulatory loop that incorporates a customized silicone left ventricle for flow visualization. The system was used to simulate the hemodynamics of a heart failure patient with an Evaheart centrifugal LVAD. The top panels show the LV with the apical inflow cannula, which is connected to the LVAD. Porcine bioprosthetic valves were used in the mitral and aortic positions, and pressure and flow measured at several locations as shown.

Figure 2. Images of the left ventricular midplane show the 2-D velocity field for the three different cannula positions at matched time points during the cardiac cycle. The velocity fields correspond to the hemodynamic conditions of Tables 1 and 2. **A**. The baseline conditions of "Pre-LVAD" are not physiological, but provide a reference state for changes with LVAD support. **B**. At an LVAD speed of 1800 rpm, a parallel flow condition is achieved in which the aortic valve is opening. **C**. At an LVAD speed of 2300 rpm, series flow conditions exist and no flow occurs through the aortic valve.

Figure 3. **A**. Two regions of interest (ROI) were defined in the apex adjacent to the inflow cannula, and the average velocity in each ROI as a function of time was calculated. ROI#1 is located on the septal side of the inflow cannula, and ROI#2 along the free wall. **B**. The cardiac cycle begins with systole, and diastole occurs at approximately 0.25 s. ROI#1 and ROI#2 were defined in the same location for each cannula position , only position C_3 is shown. **C**. Average velocity (± standard deviation) in each ROI over the cardiac cycle.

Figure 4. Pulsatility index, defined as the velocity range (maximum – minimum) for each point in the LV midplane normalized by the mean for the entire LV, shown as a color map for a single cardiac cycle. A. Parallel flow condition at an LVAD speed of 1800 rpm. B. Series flow condition at an LVAD speed of 2300 rpm. The apical regions adjacent to the cannula experience low pulsatility for all cannula positions.

Figure 5. Time series of vortex circulation for each cannula position over the cardiac cycle. The large anterior vortex generated during diastole produces a large increase in clockwise (CW) circulation, while the smaller, counter-clockwise (CCW) posterior vortex results in a negative circulation.

Appendix

While a universal vortex identification scheme has yet to be established, currently, the most popular schemes for isolating vortex cores are based on point-by-point evaluation of velocity gradient tensor, $\nabla \boldsymbol{v}(\boldsymbol{x}, \boldsymbol{y})$ [37]. $\nabla \boldsymbol{v}$ measures the change in velocity in both *x* and *y* directions at each point of the flow field relative to the neighboring points, where

$$\nabla \boldsymbol{v} = \begin{bmatrix} \frac{\partial Vx}{\partial x} & \frac{\partial Vx}{\partial y} \\ \frac{\partial Vy}{\partial x} & \frac{\partial Vy}{\partial y} \end{bmatrix}$$

The Q-criterion described by Hunt et al [Hunt 1988] is used to identify the boundary of the vortex cores. This scheme defines the vortex of interest in the velocity field where the second invariant of $\nabla \boldsymbol{v}$, Q, is greater than a positive threshold, Q_{th}. For an incompressible, 2-dimensional flow field, the second invariant is simplified and expressed as the following

$$Q = -\frac{1}{2}\left(\frac{\partial Vx}{\partial x}^2 + 2\frac{\partial Vx}{\partial y}\frac{\partial Vy}{\partial x} + \frac{\partial Vy}{\partial y}^2 \right)$$

and Q_{th} defined as the standard deviation of Q. Contiguous pixels that meet the threshold are labeled either clockwise or counterclockwise based on the sign of their vorticity, $\boldsymbol{\omega}(x,y)$, which is a measure of the rate of rotation of a fluid element:

$$\omega(x, y) = \nabla \times v(x, y)$$

The large, coherent vortex cores are then fit with an elliptical contour which provides a boundary for the area *A* used for calculating the vortex properties. The instantaneous position, radius, circulation and KE of the identified vortex cores were computed from the zero-, first-, and second order moments of the vorticity distribution, respectively, at each time point[38] [19]. Circulation and KE were defined as[38]

$$\Gamma = \int_A \omega(x, y)\, dA$$

$$KE = \frac{1}{2}\rho\int_A \mathbf{v}(x,y)^2\, dA \ ,$$

where ρ is the fluid density. The position of the vortex centroid was defined as:

$$\begin{pmatrix} x_C \\ y_C \end{pmatrix} = \frac{1}{\Gamma}\int_A \omega(x,y)\begin{pmatrix} x \\ y \end{pmatrix} dA$$

The vortex core was fit to an ellipse with axes given by the second order moments of the vorticity distribution

$$\mathsf{O} = \frac{1}{\Gamma}\int_A \omega(x,y)\begin{bmatrix} (x-x_C)^2 & (x-x_C)(y-y_C) \\ (x-x_C)(y-y_C) & (y-y_C)^2 \end{bmatrix} dA$$

such that the eigenvalues and eigenvectors of the matrix O provide the major and minor axes of the ellipse, n and n , and their orientation. The effective radius of the vortex was defined as [19]:

$$R = \sqrt{ab} \ .$$

The results were made independent of the threshold applied to the Q criterion, Q_{th}, by recomputing the vortex properties over the area defined by an ellipse centered at (x_c, y_c) and with major and minor axes given by 2n and 2n , and the aspect ratio taken as the ratio. This procedure was repeated iteratively until the vortex radius varies by less than 1% between iterations, which was usually achieved in 4-5 steps.

Table 1: Mean and cyclic hemodynamics

Cannula Position	LVAD Speed krpm	Max AoP mmHg	Min AoP mmHg	Mean AoP mmHg	Max Q_{Ao} L/min	Min Q_{Ao} L/min	Mean Q_{Ao} L/min	Aortic PI	Max Q_{LVAD} L/min	Min Q_{LVAD} L/min	Mean Q_{LVAD} L/min	LVAD PI
C_1	0	137	37	59.4	18.6	0	3.45	5.4	-	-	0.00	-
C_2	0	139	37	57.9	16.4	0	3.40	4.8	-	-	0.00	-
C_3	0	130	34	56.9	17.3	0	3.36	5.2	-	-	0.00	-
C_1	1.8	138	62	79.9	16.4	0.5	4.44	3.6	8.0	0.6	3.36	2.2
C_2	1.8	137	61	80.0	14.7	0.5	4.15	3.4	7.9	0.9	3.29	2.1
C_3	1.8	125	64	80.0	13.5	0.5	4.20	3.1	7.8	1.1	3.51	1.9
C_1	2.3	144	95	113.2	12.2	2.2	5.41	1.9	10.6	3.0	5.47	1.4
C_2	2.3	143	97	112.9	11.3	2.4	5.23	1.7	10.4	3.0	5.34	1.4
C_3	2.3	133	102	112.1	10.3	3.2	5.31	1.4	9.8	3.4	5.33	1.2

Table 2: Vortex properties from the PIV studies compared with published clinical values[19]

Parameter	**Healthy**[19]	**DCM**[19]	**PIV C_1**	**PIV C_2**	**PIV C_3**
Circulation ($x10^{-3}$ m^2/s) - CW	9.2 ± 3.6	14.4 ± 4.6	21.1	21.1	15.7
Circulation ($x10^{-3}$ m^2/s) - CCW	-5.5 ± 0.5	-8.1 ± 0.7	-10.1	-14.3	-11.7
KE (J/m) - CW	8.0 ± 4.0	14.0 ± 8.0	24.3	21.0	9.4
KE (J/m) - CCW	5.0 ± 5.0	7.0 ± 8.0	8.3	20.5	8.4
Radius (cm) - CW	0.90 ± 1.10	1.10 ± 0.30	0.65	0.66	0.74
Radius (cm) -CCW	0.54 ± 0.74	0.66 ± 0.55	0.46	0.65	0.75

CW, Clockwise; CCW, Counter-Clockwise; DCM Dilated Cardiomyopathy; KE, Kinetic Energy; PIV, Particle Image Velocimetry

Figure 1

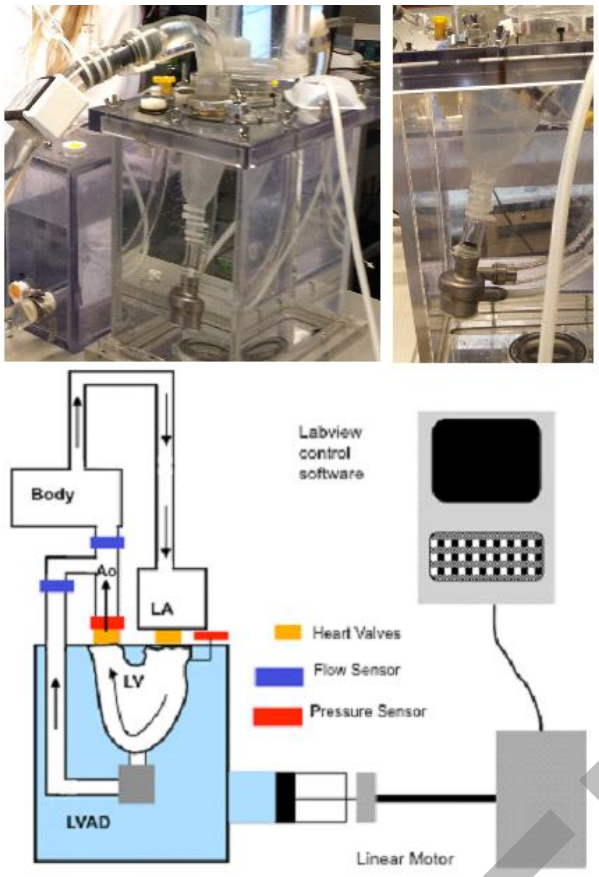

Figure 2a

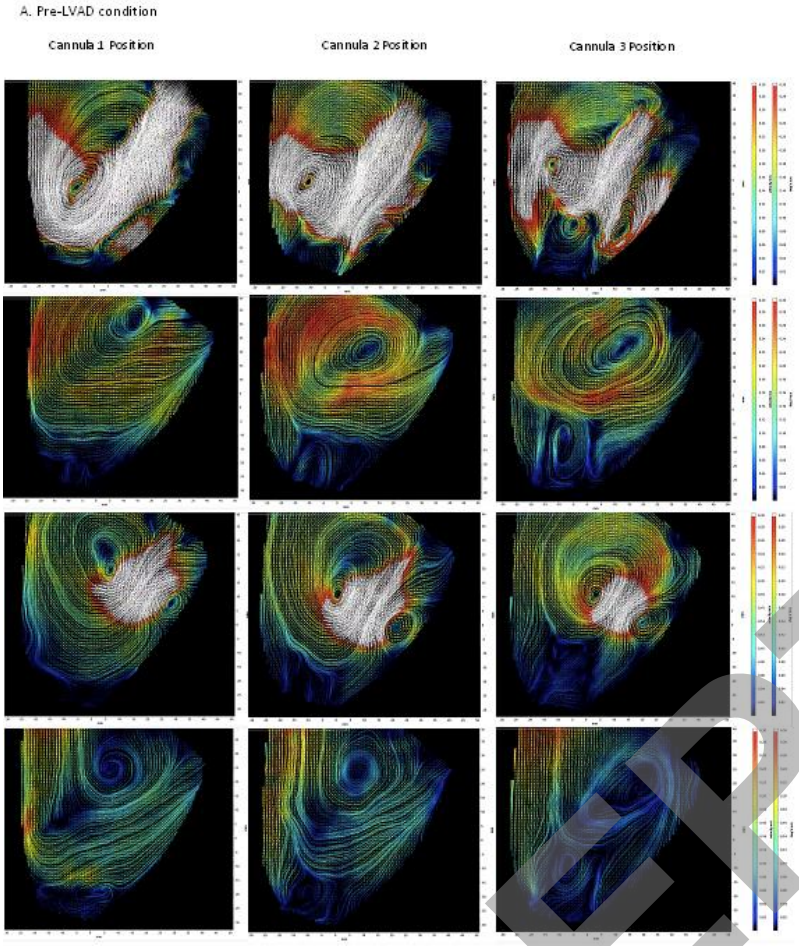

Figure 2b

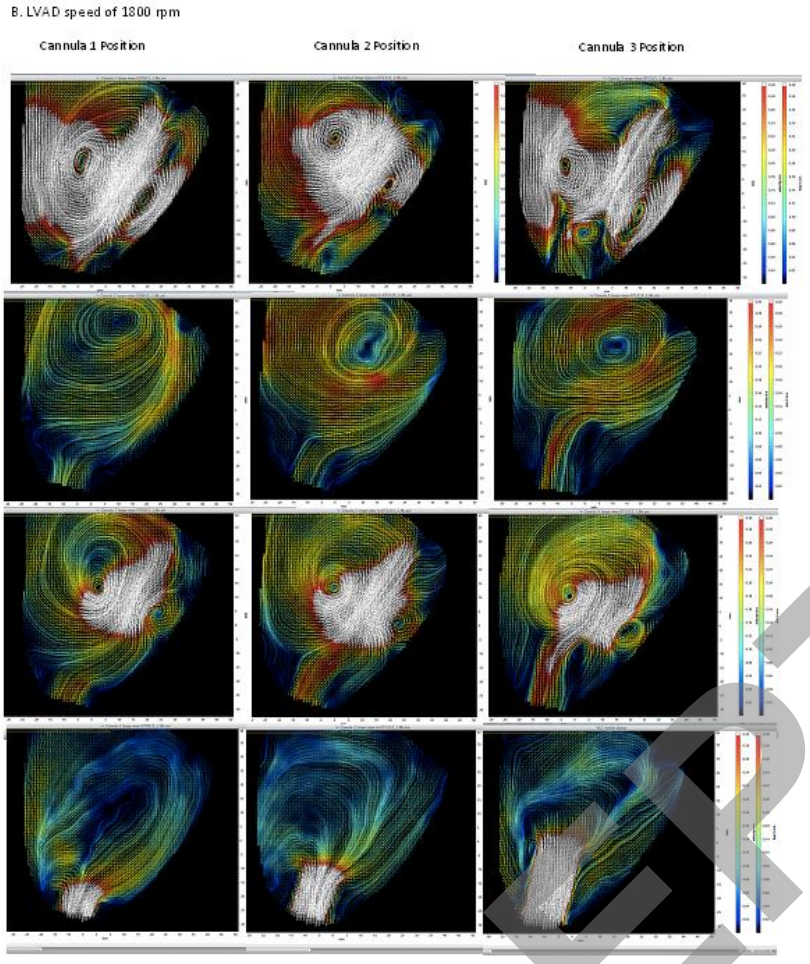

Figure 2c

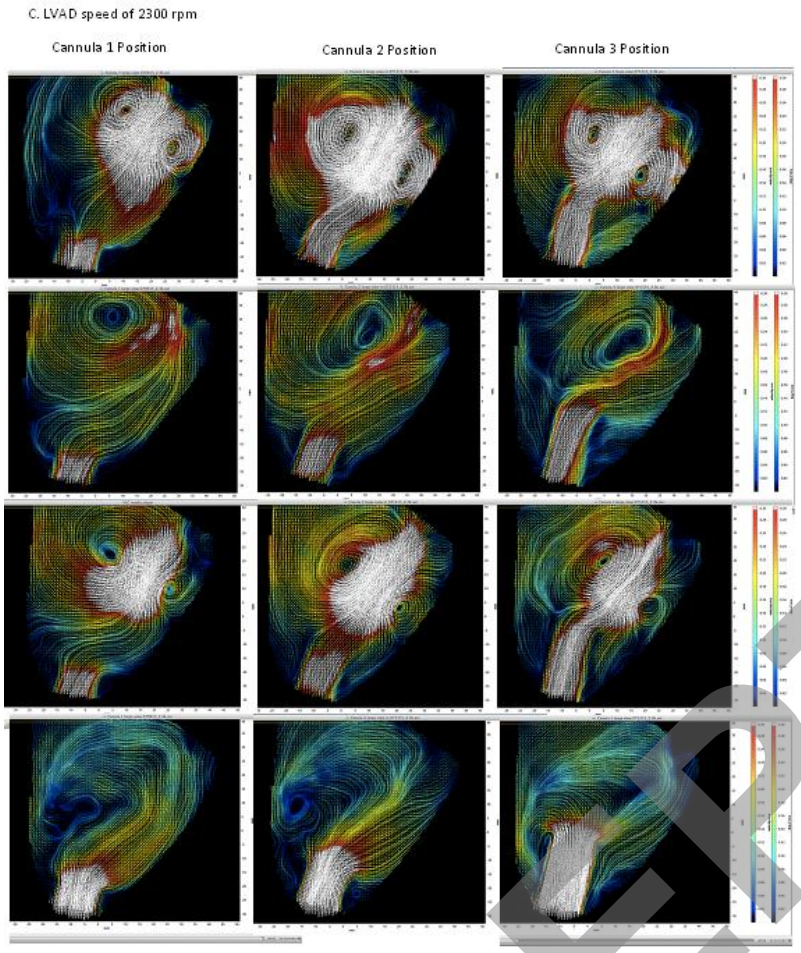

Figure 3

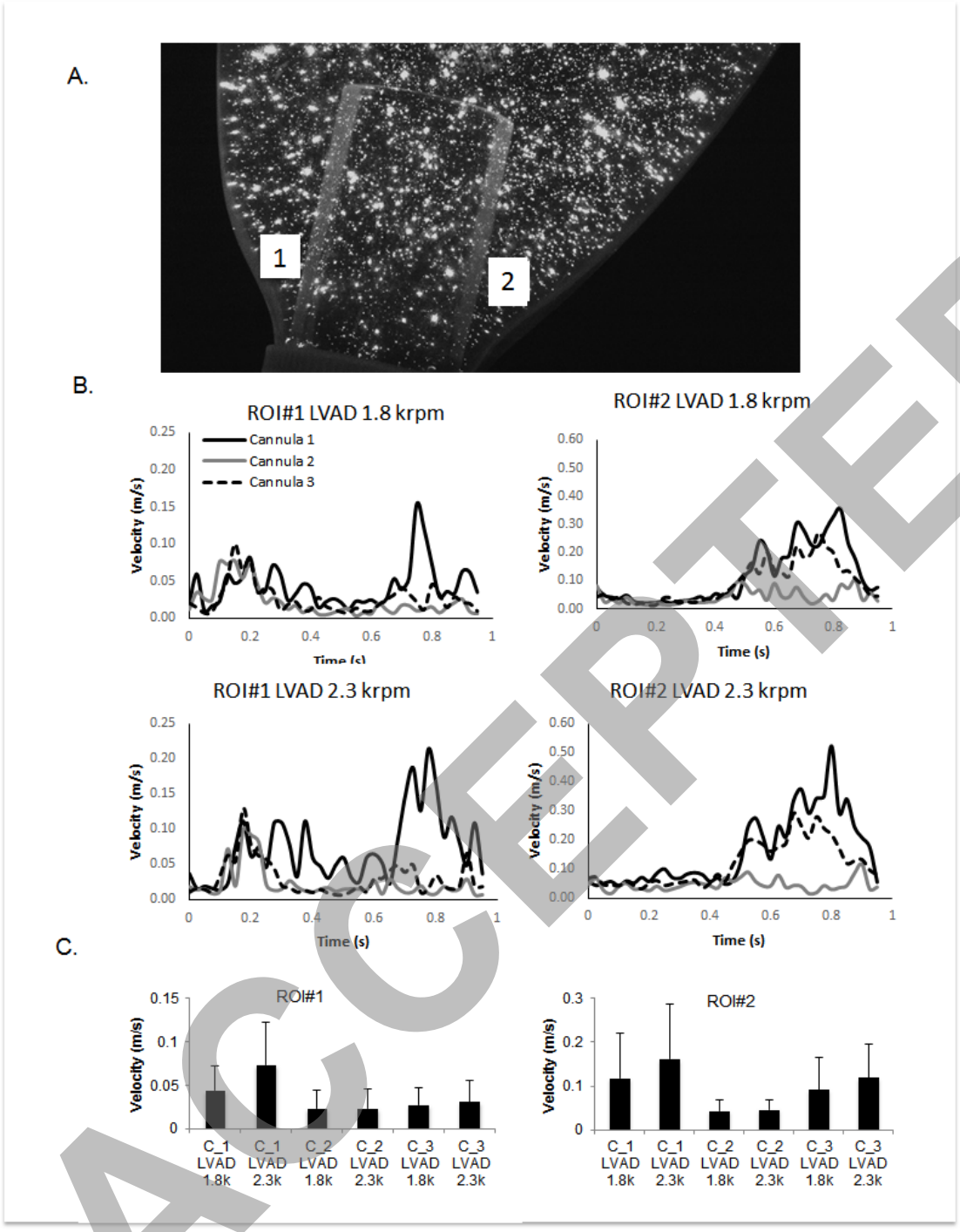

Figure 4a

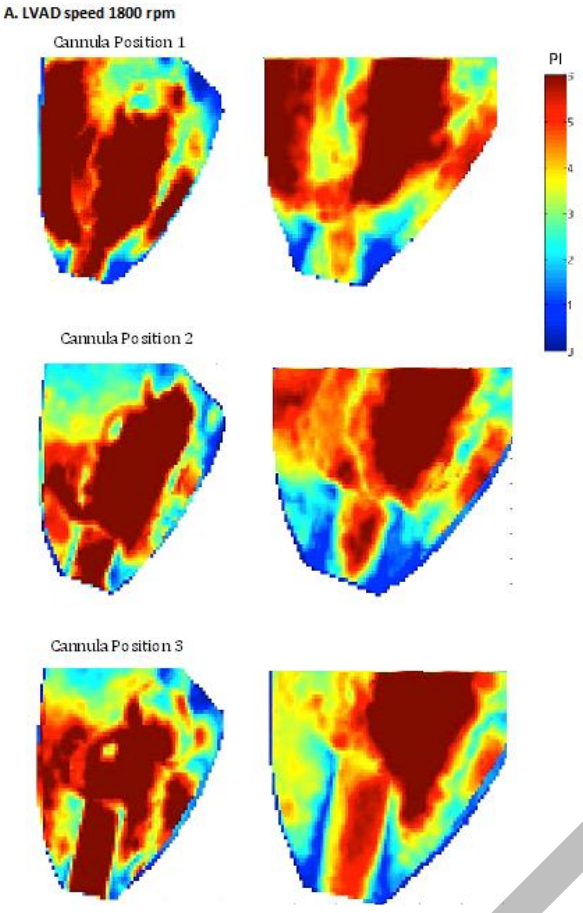

Figure 4b

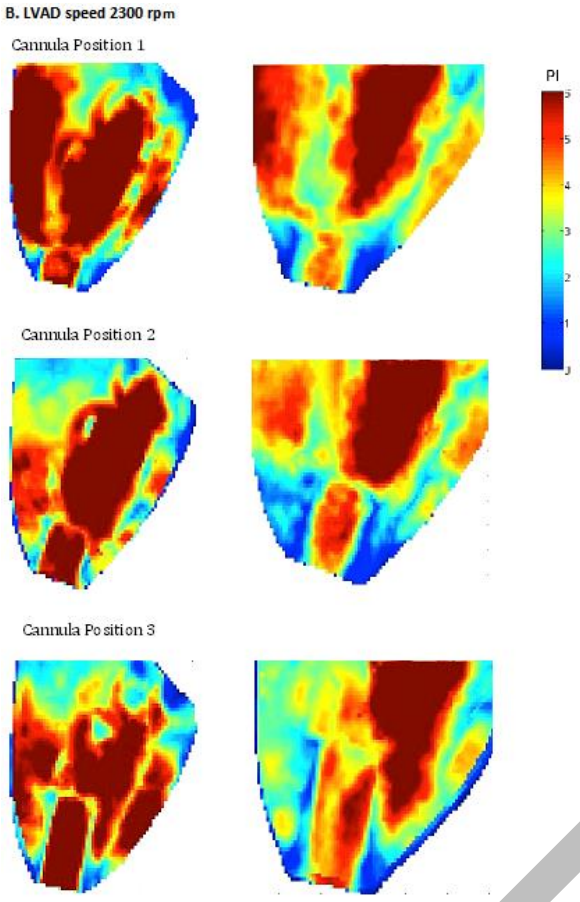

Figure 5